Predictive Model for Wall-Bounded Turbulent Flow

I. Marusic *et al.*

Science **329**, 193 (2010);
DOI: 10.1126/science.1188765

Science (print ISSN 0036-8075; online ISSN 1095-9203) is published weekly, except the last week in December, by the American Association for the Advancement of Science, 1200 New York Avenue NW, Washington, DC 20005.

strain field, whereas the typical length of the filaments is determined by the strength of disorders. Interestingly, discernible anisotropy is seen in that the "nematic" domains along the [1$\bar{1}$0] direction are statistically more favorable than the [001] direction, in fair agreement with the transport anisotropy observed in control samples (*21*) (fig. S9). In the strained NSMO/(110)STO films, the in-plane lattice constant is locked to that of the substrate along the [001] direction while relaxed along the [1$\bar{1}$0] direction (*23*, *24*). At the same time, the charge-ordered planes are parallel to the (100) or (010) planes. Because the low-*T* CMR effect is accompanied by lattice deformation (*22*), the metallic domains may tend to expand along the more strain-free axis, resulting in the in-plane anisotropy. The nematic phase at this length scale provides a contrasting framework to understand the "stripe" phenomenon that also breaks in-plane C_2 symmetry at much shorter length scales (*31*).

The physical picture depicted above is further corroborated by results combining both *T* (*21*) (fig. S10) and *H*. In particular, by using a field-cool (FC) process, we can access states with much lower ρ than the zero-field-cool (ZFC) process discussed so far. Figure 3, A and B, shows the FC curves at four different fields and the corresponding microwave images taken at 12 K, which is below T_{COO} for all fields. The continuous COO-I phases at FC-2T break into isolated micrometer-sized domains at FC-7T, which continue to be percolated through by FM-M filaments at FC-8T and shrink down to small droplets at FC-9T. Taking the transport signatures T_C and T_{COO}, we construct the phase diagram of this NSMO/STO sample in Fig. 3C, where phase coexistence is denoted below T_{COO}. This phase diagram is reminiscent of the one for single-crystal NSMO (*22*) except that the reentrant behavior reported there is beyond our field range. By using MIM, we can directly study the microscopic origin of the hysteresis. In Fig. 3C, two paths arriving at the same external conditions are shown: the ZFC process from 200 K to 20 K followed by a field sweep to 6 T, or field sweep to 6 T at 200 K before FC to 20 K (*21*) (fig. S11). The two MIM images in Fig. 3D display remarkably different percolating networks. For the high-ρ (1.4 ohm·cm) ZFC state, glassy FM-M filaments are observed in the COO-I background. For the low-ρ (0.02 ohm·cm) FC state, on the other hand, the FM-M phases occupy a much larger portion and even form micrometer-sized puddles elongated in the [1$\bar{1}$0] direction. Although hysteresis during the low-T CMR effect is known in single-crystal NSMO from bulk measurements, tools like MIM enable real-space electrical imaging and demonstrate the strong dependence of phase separation on local disorders and strain fields near the multiphase boundary.

References and Notes

1. E. Dagotto, *Science* **309**, 257 (2005).
2. Y. Tokura, *Rep. Prog. Phys.* **69**, 797 (2006).
3. S. Yunoki *et al.*, *Phys. Rev. Lett.* **80**, 845 (1998).
4. M. Vershinin *et al.*, *Science* **303**, 1995 (2004); published online 12 February 2004 (10.1126/science.1093384).
5. T. Hanaguri *et al.*, *Nature* **430**, 1001 (2004).
6. C. Howald, H. Eisaki, N. Kaneko, M. Greven, A. Kapitulnik, *Phys. Rev. B* **67**, 014533 (2003).
7. N. D. Mathur, P. B. Littlewood, *Solid State Commun.* **119**, 271 (2001).
8. K. H. Ahn, T. Lookman, A. R. Bishop, *Nature* **428**, 401 (2004).
9. J. Burgy, A. Moreo, E. Dagotto, *Phys. Rev. Lett.* **92**, 097202 (2004).
10. A. Moreo, M. Mayr, A. Feiguin, S. Yunoki, E. Dagotto, *Phys. Rev. Lett.* **84**, 5568 (2000).
11. M. Fäth *et al.*, *Science* **285**, 1540 (1999).
12. Ch. Renner, G. Aeppli, B.-G. Kim, Y. A. Soh, S. W. Cheong, *Nature* **416**, 518 (2002).
13. L. Zhang, C. Israel, A. Biswas, R. L. Greene, A. de Lozanne, *Science* **298**, 805 (2002); published online 19 September 2002 (10.1126/science.1077346).
14. W. Wu *et al.*, *Nat. Mater.* **5**, 881 (2006).
15. J. C. Loudon, N. D. Mathur, P. A. Midgley, *Nature* **420**, 797 (2002).
16. M. Uehara, S. Mori, C. H. Chen, S.-W. Cheong, *Nature* **399**, 560 (1999).
17. K. Lai, W. Kundhikanjana, M. Kelly, Z. X. Shen, *Rev. Sci. Instrum.* **79**, 063703 (2008).
18. K. Lai, W. Kundhikanjana, M. Kelly, Z. X. Shen, *Phys. Lett.* **93**, 123105 (2008).
19. B. T. Rosner, D. W. van der Weide, *Rev. Sci. Instrum.* **73**, 2505 (2002).
20. Z. Wang *et al.*, *J. Appl. Phys.* **92**, 808 (2002).
21. Materials and methods are available as supporting material on *Science* Online.
22. H. Kuwahara, Y. Tomioka, A. Asamitsu, Y. Moritomo, Y. Tokura, *Science* **270**, 961 (1995).
23. H. Aliaga *et al.*, *Phys. Rev. B* **68**, 104405 (2003).
24. M. Nakamura, Y. Ogimoto, H. Tamaru, M. Izumi, K. Miyano, *Appl. Phys. Lett.* **86**, 182504 (2005).
25. Y. Wakabayashi *et al.*, *Phys. Rev. Lett.* **96**, 017202 (2006).
26. T. Higuchi *et al.*, *Appl. Phys. Lett.* **95**, 043112 (2009).
27. D. D. Sarma *et al.*, *Phys. Rev. Lett.* **93**, 097202 (2004).
28. J. Tao *et al.*, *Phys. Rev. Lett.* **103**, 097202 (2009).
29. S. Kirkpatrick, *Rev. Mod. Phys.* **45**, 574 (1973).
30. M. Mayr *et al.*, *Phys. Rev. Lett.* **86**, 135 (2001).
31. J. A. Robertson, S. A. Kivelson, E. Fradkin, A. C. Fang, A. Kapitulnik, *Phys. Rev. B* **74**, 134507 (2006).

32. We thank X.-L. Qi, Y. Chen, J. C. Davis, and S. A. Kivelson for valuable discussions. The work is supported by NSF (grants DMR-0906027 and Center of Probing the Nanoscale PHY-0425897), Department of Energy (DE-FG03-01ER45929-A001), Funding Program for World-Loading Innovative R and D on Science and Technology (FIRST) of Japan Society for the Promotion of Science (JSPS), and King Abdullah University of Science and Technology Fellowship (KUS-F1-033-02). Stanford University has filed a patent application with the U.S. Patent Office on the AFM compatible microwave imaging technique. This technology was modified for low-temperature measurement in this report.

Supporting Online Material

www.sciencemag.org/cgi/content/full/329/5988/190/DC1
Materials and Methods
Figs. S1 to S11

22 March 2010; accepted 3 June 2010
10.1126/science.1189925

Predictive Model for Wall-Bounded Turbulent Flow

I. Marusic,* R. Mathis, N. Hutchins

The behavior of turbulent fluid motion, particularly in the thin chaotic fluid layers immediately adjacent to solid boundaries, can be difficult to understand or predict. These layers account for up to 50% of the aerodynamic drag on modern airliners and occupy the first 100 meters or so of the atmosphere, thus governing wider meteorological phenomena. The physics of these layers is such that the most important processes occur very close to the solid boundary—the region where accurate measurements and simulations are most challenging. We propose a mathematical model to predict the near-wall turbulence given only large-scale information from the outer boundary layer region. This predictive capability may enable new strategies for the control of turbulence and may provide a basis for improved engineering and weather prediction simulations.

Flow over a solid surface or wall produces a region of strong shear due to the no-slip condition at the surface. This strong shear induces tangential stresses at the surface, which, from an engineering perspective, will lead to energy expenditure (drag for aerodynamic and hydrodynamic vehicles, increased pumping requirements for pipe networks, etc.). Under most practical conditions, this thin region of shear—known as a boundary layer—is turbulent; the fluid motion is no longer well ordered and instead succumbs to highly chaotic motions, leading to further increases in mechanical losses. Up to half of the fuel burned by a modern airliner during flight is used to overcome drag due to turbulent boundary layers (this proportion is higher still for a large oil tanker or submarine). In addition to energy expenditure, turbulent boundary layers also promote increased mixing, heat transfer, and exchange processes; thus, when they occur on an atmospheric scale, they have important meteorological and climatological implications.

A long-standing challenge has been to understand and predict the behavior of wall-bounded turbulence, especially because the ability to predict

Department of Mechanical Engineering, University of Melbourne, Victoria 3010, Australia.

*To whom correspondence should be addressed. E-mail: imarusic@unimelb.edu.au

such behavior often implies opportunities for control (*1*). Such aspirations were strengthened by the discovery during the 1950s and 1960s that turbulent boundary layers, despite their obvious disorder, possess certain recurrent features or coherent patterns, and recent studies have considerably expanded this view (*2*). Our current work uses recently acquired knowledge of large-scale recurrent features to build a predictive model for the complex small-scale motions that occur very close to the surface. Under typical practical conditions, this important near-wall region is often beyond the scrutiny of experimental measurement techniques and therefore remains largely undocumented. The current model provides a basis for predicting flows in the near-wall region, where data would otherwise be unavailable, using only information gathered farther away from the surface. In addition to offering valuable insight into the complex physics of wall-bounded turbulence, the model could also have ramifications for the simulation of these flows.

Computer simulations of wall-bounded turbulence are extremely challenging because the simulation must resolve the entire range of scales of turbulent motion (*3*). For a boundary layer that has developed over the length of a large aircraft fuselage, these motions could range from the meter scale down to just a few micrometers for the smallest dissipative motions. Atmospheric surface layers will have similar scale separation, with the largest scales on the order of 1 km and the smallest around 1 mm. In general, turbulent boundary layers are characterized by the dimensionless parameter known as the Reynolds number (*Re*), which is essentially the ratio of the largest inertial scale to the smallest dissipative scale in the flow. To date, even the largest supercomputers can solve such flows only at comparatively low *Re* values, which are several orders of magnitude below most practical applications. In overcoming this limitation, one approach has been large-eddy simulation (*4*), in which a sparse grid is used to resolve the large-scale motions, whereas the unresolved small-scale motions are modeled. For high-*Re* wall-bounded flows, this also requires a near-wall model to account for the relationship between the wall shear stress and the outer-layer flow (*5*). This current work aims to improve our understanding of this complex interaction, offering a simple mathematical model that can accurately predict near-wall turbulent statistics based only on large-scale outer-layer information.

For wall turbulence, the most relevant Reynolds number is $Re_\tau = \delta U_\tau/\nu$ (known as the friction Reynolds number or Karman number), which is a ratio of the inner and outer length scales. Here, the outer scale is δ, the boundary layer thickness, which corresponds to the normal distance from the wall (beyond which the velocity recovers to the free stream). The inner length scale is ν/U_τ, where ν is the kinematic viscosity and $U_\tau = (\tau_0/\rho)^{1/2}$ is the friction velocity, where τ_0 is the mean wall-shear stress and ρ is the fluid density.

The classical view is that the inner region is taken nominally to be $0 < z^+ < 0.15Re_\tau$, where z is the distance normal to the wall and the superscript + denotes normalization with inner variables (i.e., $z^+ = zU_\tau/\nu$, $U^+ = U/U_\tau$, etc). The outer region is nominally taken to be $30/Re_\tau < z/\delta < 1$, and the overlap of the inner and outer regions is referred to as the logarithmic layer, as here the mean streamwise (x-direction) velocity nominally follows a log-law formulation (*6*). These different regions, or layers, are illustrated schematically in the left panel of Fig. 1. The near-wall inner region (say, $0 < z^+ < 30$) in the classical description is taken to be independent of the outer region, and all the turbulence statistics U^+, $\overline{u^{2}}^{+}$, $\overline{u^{3}}^{+}$, etc., are universal functions of z^+. Here, U and u are the mean and fluctuating streamwise velocities, respectively, and overbars denote ensemble time-averaged quantities. A number of studies have challenged this classical description in recent years, showing evidence that the inner region has a dependence on *Re*, and thus on the outer length scale δ (*7*–*10*).

Recent studies conducted at higher values of *Re* have also noted the presence of very-large-scale motions (VLSMs, also referred to as "superstructures") in the logarithmic layer of turbulent boundary layers (*11*–*13*). Our understanding of these features is somewhat nascent, yet in general they can be categorized as very large elongated regions of negative velocity fluctuation (with instantaneous reported lengths of 15δ to 20δ), flanked on either side in the spanwise direction by regions of positive fluctuation. These regions are inclined slightly to the horizontal (such that the downstream end extends farther from the wall) and, in a mean sense, are accompanied by large-scale counterrotating roll modes. These elongated features meander, or appear sinuous, in the streamwise direction and in general seem to be ubiquitous for all high-*Re* wall-bounded turbulence. They have been noted in high-*Re* pipe, channel, and flat-plate turbulent boundary layers, as well as in the atmospheric surface layer (where they are on the kilometer scale) (*9*, *13*–*15*). The sketch in the upper left of Fig. 1 shows a conceptual view of these events (where red and blue represent positive and negative fluctuations of u, respectively). Although these events seem to be primarily centered (and most energetic) in the logarithmic region, they have an influence that extends to the wall, and a large-scale fluctuation (or footprint) is superimposed on the near-wall turbulence. This is as predicted by Townsend's attached-eddy hypothesis (*16*). However, in addition to this superimposition of energy, the superstructure events also modulate the magnitude of the small-scale fluctuations (*12*, *17*). Within a large-scale low-speed event (the blue region of Fig. 1), it is found that close to the wall the small-scale fluctuations are attenuated, while farther away from the wall the small-scale fluctuations are amplified above

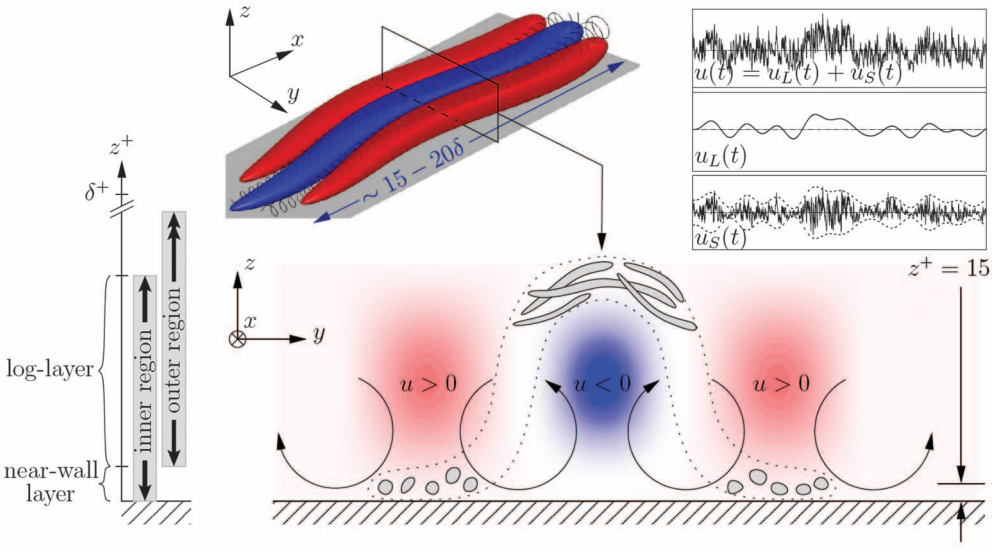

Fig. 1. Schematic of organized coherent flow motion known as a superstructure and its interaction across the turbulent boundary layer. These very-large-scale motions extend from the log region down toward the wall, both superimposing their signature and modulating the near-wall region. The sample u time series highlight the modulation effect of the large scales on the small scale at $z^+ = 15$; the near-wall location corresponds to the peak turbulence intensity. The features shown in gray indicate elongated filamentary vortex structures and their conjectured alignment with the superstructure.

background levels. The reverse scenario is noted in the red regions of Fig. 1 (in the large-scale regions of positive u). This observation is represented in the upper right plot of Fig. 1, where a sample instantaneous fluctuating time signal of streamwise velocity $u(t)$ is shown at a location near the wall (at $z^+ = 15$, close to the peak in turbulence production). The two lower plots show the signal spectrally decomposed into large-scale (u_L) and small-scale (u_S) components, where u_L contains only energy with $\lambda_x > \delta$ and u_S has energy with $\lambda_x < \delta$ (where λ_x is streamwise wavelength). It is apparent from the signal of u_S (bottom plot) that the small-scale fluctuations are modulated by an envelope that is well described by the large-scale signal (u_L) (*17*). Close to the wall, the small-scale fluctuations are attenuated within negative u_L and amplified within positive u_L. Recently (*17*) we showed that u_L is highly correlated with the large-scale velocity signal in the log region (u_{OL}), and thus the large-scale "superstructure" events modulate the near-wall scales in a manner akin to amplitude modulation. Farther from the wall, the sign of the correlation between u_L and the envelope of u_S reverses, such that for $z^+ \geq 3.9(Re_\tau)^{1/2}$ the small-scale fluctuations are increased within negative large-scale events (and reduced within positive large-scale events). The crossover position $3.9(Re_\tau)^{1/2}$ was empirically determined, but such a scaling is consistent with the geometric center of the log layer (*17*). The bottom plot of Fig. 1 shows an overview of this modulation scenario. The blue and red regions show a cross section through the elongated low- and high-speed superstructure events, with associated counterrotating roll modes also shown. The modulation is represented by the gray contours highlighting the increased small-scale vortical activity close to the wall beneath the high-speed (red) regions, and also farther away from the wall within the low-speed (blue) regions.

If one accepts the amplitude modulation effect as the mechanism linking the large-scale superstructures to the behavior of the near-wall region, then this leads to the possibility that a simple mathematical model may be devised that captures this interaction. This is very desirable, as it would allow prediction of the fluctuating velocity statistics in the near-wall region given only information about the large-scale signal in the log region. Such a model can be expressed as

$$u_P^+ = u^*(1 + \beta u_{OL}^+) + \alpha u_{OL}^+ \qquad (1)$$

where u_P^+ is the predicted u signal at z^+, u_{OL} is the fluctuating large-scale signal from the log region, u^* is the statistically "universal" signal at z^+ (normalized in wall units), and α and β are, respectively, the superimposition and modulation coefficients. Note that the model consists of two parts; the first part, $u^*(1 + \beta u_{OL}^+)$, models the amplitude modulation at z^+ by the large-scale motions, and the second part, αu_{OL}^+, models the superimposition of the large-scale motions felt at z^+.

The large-scale signal, u_{OL}, is the only user input required for Eq. 1 and is obtained from the u signal in the log region (at a given z/δ value) involving two steps. First, the u signal is low-pass filtered to retain only large scales (here, streamwise wavelengths of $\lambda_x^+ > 7000$ are retained), and second, because we are equating a log-region signal (from z_O^+) to a specified position z^+, the measured u signal phase information is retained and the signal is shifted to account for the structure inclination angle, θ_{LS}, between these two wall-normal positions, which previous studies have shown to be effectively invariant with Re (*18*, *19*). Figure 2 shows a sample of a measured u_{OL}^+ signal together with the corresponding simultaneously measured u signal at $z^+ = 15$. Note the high degree of correlation of u_{OL}^+ with the low-frequency content of u^+ (z^+).

The procedure for finding u^*, α, β, and θ_{LS} is as follows: An experiment was conducted at $Re_\tau = 7300$ that involved simultaneously sampling u signals from two hot wires mounted at z_O^+ and z^+ (*20*). z_O^+ was fixed nominally in the center of the classical log region, which corresponds to $z_O^+ = 3.9(Re_\tau)^{1/2}$ (*17*), whereas z^+ could be traversed within the range $0 < z^+ < z_O^+$. The modulation coefficient β was found by using Eq. 1 and optimizing the value of β that returned a u^* signal with no amplitude modulation. Thus, the value of β that returns an unmodulated u^* signal was determined to be the universal value with the corresponding u^* as the universal signal. The structure inclination angle, θ_{LS}, corresponds to the time delay that locates the maximum in a cross-correlation between the large-scale u signals at z_O^+ and z^+, and α corresponds to the value of the maximum cross-correlation coefficient between these signals. These are taken as invariants, and therefore α, β, and θ_{LS} are functions only of z^+, and u^* is a universal function of t^+ at a given z^+ level. Time-series data files of u^* together with its large-scale phase information are available from the authors, as are corresponding tabulated values of α, β, and θ_{LS}. The $u^*(z^+, t^+)$ signals are records over a nondimensional time of $T^+ = 4.55 \times 10^6$, which means that they are sufficiently long to ensure a statistically representative realization (*21*). With u^*, α, and β known and fixed for a given wall-normal position, prediction of u_P^+ can now be made using Eq. 1 where the only input is the large-scale u signal at z_O^+.

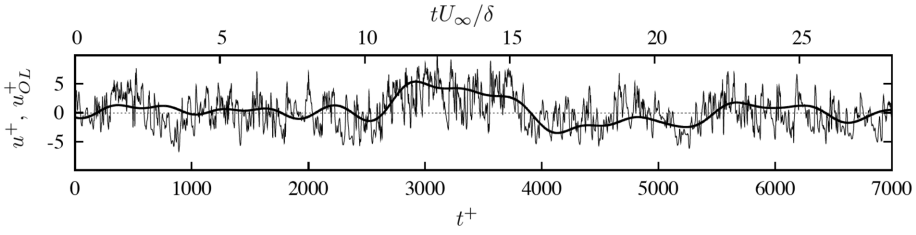

Fig. 2. Example of fluctuating signal u^+ at $z^+ = 15$ and large-scale fluctuating component u_{OL}^+ in the outer layer (thick blank line) at $z^+ = 330$ measured in a turbulent boundary layer at $Re_\tau = 7300$.

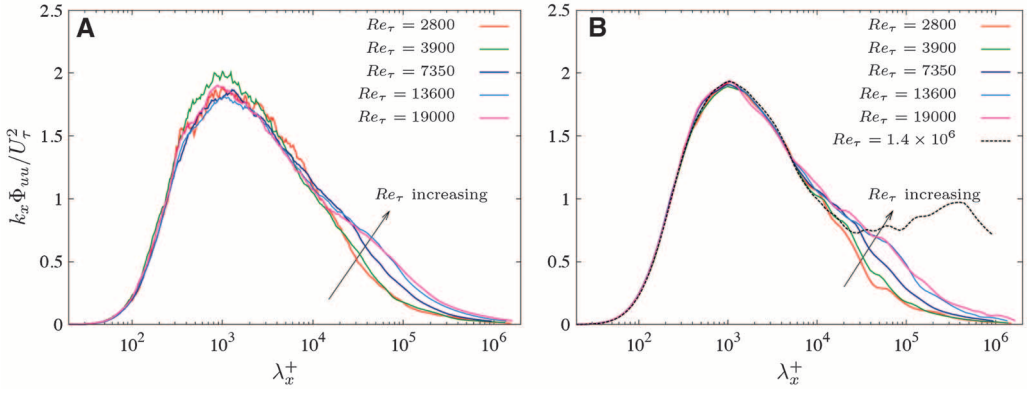

Fig. 3. (**A** and **B**) Reynolds number evolution of the premultiplied energy spectra of streamwise velocity at the inner-peak location ($z^+ = 15$) for the true measurements (A) and the prediction based on the filtered u signal measured in the log region (B).

The experimental data were obtained in the Melbourne High Reynolds Number Boundary Layer Facility, a wind tunnel that obtains high values of *Re* with very low free-stream turbulence levels (<0.05%) over a flat plate of 27 m length (*22*, *23*). The boundary layer thickness at x = 21 m is in excess of 300 mm, allowing for excellent spatial and temporal resolution (*21*). The velocity signatures are obtained by hot-wire anemometry; full details of the experimental setup are given in (*17*). Single hot-wire measurements were also carried out at five values of Re_τ (2800, 3900, 7300, 13,600, and 19,000), and these provide the profiles against which predictions can be validated. For the predictions of these experiments, only the large-scale filtered velocity signal measured at $z_O^+ = 3.9(Re_\tau)^{1/2}$ is used to provide the u_{OL} input to Eq. 1, from which predicted velocity signals can be calculated at any wall-normal position [in the range $0 < z^+ < 3.9(Re_\tau)^{1/2}$]. Thus, all near-wall fluctuating signals are recreated on the basis of a single log-region measurement. Comparison is also made here to data at $Re_\tau = 1.4 \times 10^6$ from experiments by the authors in the atmospheric surface layer on the salt flats of the Utah Western Desert using a wall-normal array of sonic anemometers (*13*, *15*).

Figures 3 and 4 show some indicative results of the prediction scheme. Figure 3B shows predictions of premultiplied spectra at $z^+ = 15$ compared to the measured results shown in Fig. 3A. Excellent agreement is seen for the available data. (Note that no comparison exists for the Utah case at this very–near-wall position.) The area under the curves in Fig. 3 corresponds to $\overline{u^2}^+$, and the measurements and predictions indicate a clear increase in the area with increasing values of *Re* resulting from the extra energy at long wavelengths. This explains the findings of previous studies (*7*–*10*, *21*) that have also noted this increase in the peak value of $\overline{u^2}^+$ with increasing *Re*. Although this result is contrary to the classical wall-scaling theories used in many commercial simulation schemes, it is consistent with the Townsend attached-eddy hypothesis (*10*). Figure 4 compares measurements and predictions for the various wall-normal positions of $\overline{u^2}^+$, together with higher-order moments. For brevity, here only the sixth-order moment is shown along with the skewness profiles. Again, excellent agreement is found for all moments up to the sixth-order moment. While the experimental uncertainty increases with the higher-order moments, the trends predicted by the model follow the experimental results well. The predictions are able to capture the change in sign of skewness in the viscous buffer region (at $z^+ \approx 30$) as *Re* increases. Previously this trend had been puzzling (*7*), but here we are able to confirm that this behavior is likely due to the modulation effect of the superstructure events in the near-wall region.

These promising results lend support to the superimposition and modulation coupling mechanism between the inner and outer regions of wall turbulence. At this stage, the model presented is for zero-pressure-gradient boundary layer flows only, but it can be extended to other flows if the corresponding two-point experiments required for u^* are carried out in those flows at any value of *Re*. Caution is indicated concerning the trends predicted by the Utah data, which are subject to larger experimental uncertainties (*24*). These data have been used to illustrate an application of the model at very high *Re*, but whether the predicted trend in Fig. 4 holds—with an outer peak in $\overline{u^2}^+$ exceeding the level of the inner peak at $z^+ \approx 15$—remains an open question.

The simple algebraic form of Eq. 1 is an ideal basis for a near-wall model for high-*Re* large-eddy simulations. These simulations rely on near-wall inputs based only on large-scale information of the velocity field in the logarithmic region (where the first grid point is typically located) (*25*–*27*). This is exactly the information that Eq. 1 provides, and future studies in this direction are continuing. Our predictive model can also be used to provide the missing information from leading high-*Re* facilities [such as in the Princeton superpipe (*28*)], where the near-wall region is largely inaccessible to measurement because of the extremely small viscous scales associated with such facilities.

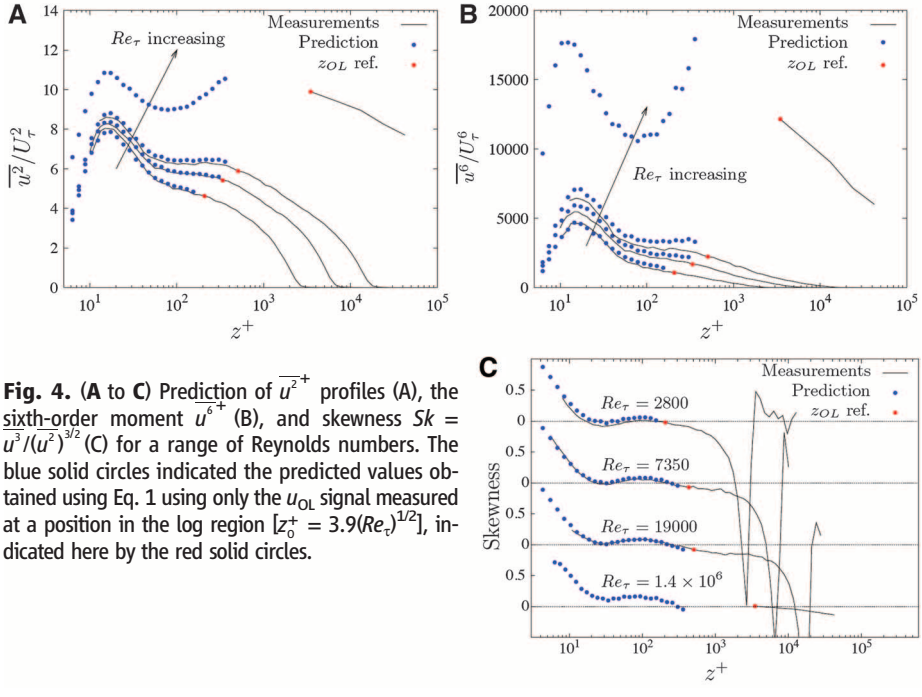

Fig. 4. (**A** to **C**) Prediction of $\overline{u^2}^+$ profiles (A), the sixth-order moment $\overline{u^6}^+$ (B), and skewness $Sk = \overline{u^3}/(\overline{u^2})^{3/2}$ (C) for a range of Reynolds numbers. The blue solid circles indicated the predicted values obtained using Eq. 1 using only the u_{OL} signal measured at a position in the log region [$z_o^+ = 3.9(Re_\tau)^{1/2}$], indicated here by the red solid circles.

References and Notes

1. B. Hof, A. de Lozar, M. Avila, X. Tu, T. M. Schneider, *Science* **327**, 1491 (2010).
2. R. J. Adrian, *Phys. Fluids* **19**, 041301 (2007).
3. P. Moin, K. Mahesh, *Annu. Rev. Fluid Mech.* **30**, 539 (1998).
4. C. Meneveau, J. Katz, *Annu. Rev. Fluid Mech.* **32**, 1 (2000).
5. U. Piomelli, *Prog. Aerosp. Sci.* **35**, 335 (1999).
6. S. B. Pope, *Turbulent Flows* (Cambridge Univ. Press, Cambridge, 2000).
7. M. M. Metzger, J. C. Klewicki, *Phys. Fluids* **13**, 692 (2001).
8. D. B. De Graaff, J. K. Eaton, *J. Fluid Mech.* **422**, 319 (2000).
9. S. Hoyas, J. Jiménez, *Phys. Fluids* **18**, 011702 (2006).
10. I. Marusic, G. J. Kunkel, *Phys. Fluids* **15**, 2461 (2003).
11. K. C. Kim, R. J. Adrian, *Phys. Fluids* **11**, 417 (1999).
12. N. Hutchins, I. Marusic, *Philos. Trans. R. Soc. London Ser. A* **365**, 647 (2007).
13. N. Hutchins, I. Marusic, *J. Fluid Mech.* **579**, 1 (2007).
14. J. Monty, J. Stewart, R. Williams, M. Chong, *J. Fluid Mech.* **589**, 147 (2007).
15. I. Marusic, N. Hutchins, *Flow Turbul. Combus.* **81**, 115 (2008).
16. A. A. Townsend, *The Structure of Turbulent Shear Flow, Vol. 2* (Cambridge Univ. Press, Cambridge, 1976).
17. R. Mathis, N. Hutchins, I. Marusic, *J. Fluid Mech.* **628**, 311 (2009).
18. I. Marusic, W. D. Heuer, *Phys. Rev. Lett.* **99**, 114504 (2007).
19. G. R. Brown, A. S. W. Thomas, *Phys. Fluids* **20**, S243 (1977).
20. Note that this experiment is conducted at an arbitrary value of *Re*.
21. N. Hutchins, T. B. Nickels, I. Marusic, M. S. Chong, *J. Fluid Mech.* **635**, 103 (2009).
22. T. B. Nickels, I. Marusic, S. M. Hafez, M. S. Chong, *Phys. Rev. Lett.* **95**, 074501 (2005).
23. T. B. Nickels, I. Marusic, S. M. Hafez, N. Hutchins, M. S. Chong, *Philos. Trans. R. Soc. London Ser. A* **365**, 807 (2007).
24. G. J. Kunkel, I. Marusic, *J. Fluid Mech.* **548**, 375 (2006).
25. I. Marusic, G. J. Kunkel, F. Porté-Agel, *J. Fluid Mech.* **446**, 309 (2001).
26. U. Piomelli, E. Balaras, *Annu. Rev. Fluid Mech.* **34**, 349 (2002).
27. D. Chung, D. I. Pullin, *J. Fluid Mech.* **631**, 281 (2009).
28. M. V. Zagarola, A. J. Smits, *J. Fluid Mech.* **373**, 33 (1998).

29. Supported by Australian Research Council grants FF0668703, DP0984577, and DP1092585.

24 February 2010; accepted 13 May 2010
10.1126/science.1188765